Journal of
Marine Science and Engineering

MDPI

Article

Spatio-Temporal Variations in Foredune Dynamics Determined with Mobile Laser Scanning

Jasper Donker *, Marcel van Maarseveen and Gerben Ruessink

Department of Physical geography, Faculty of Geosciences, Utrecht University, Princetonlaan 8a, 3508 TC Utrecht, The Netherlands; M.C.G.vanMaarseveen@uu.nl (M.v.M.); b.g.ruessink@uu.nl (G.R.)
* Correspondence: j.j.a.donker@uu.nl

Received: 2 October 2018; Accepted: 24 October 2018; Published: 30 October 2018

Abstract: Coastal foredunes are highly dynamic landforms because of rapid erosion by waves and currents during storm surges in combination with gradual accretion by aeolian transport during more quiescent conditions. While our knowledge into the mechanisms behind foredune erosion have reached considerable maturity, this is not the case for foredune growth. High resolution spatio-temporal data sets of beach and foredune topography, which are needed to increase our understanding of mechanisms behind aeolian transport in coastal environments and to develop predictive dune-accretion models, are scarce. Here we aim to illustrate that repeated Mobile Laser Scanning (MLS) surveys provide an accurate and robust method to study detailed changes in dune volume on the timescales of months to years. An MLS system attached to an inertial navigation system with RTK-GPS (INS-GPS) was used to carry out 13 surveys along a 3.5-km Dutch beach over a 2.5-year period. The height observations were post-processed and averaged into 1 $\times$ 1 m Digital Elevation Models (DEMs). Comparison with airborne LiDAR and RTK-GPS data revealed that the obtained DEMs were accurate and robust up to a height of 15 m in the foredune above which dense vegetation hampers the MLS to see the sand surface. Estimates of dune volume change of the lower 13 m of the foredune have an uncertainty of about 0.25 m^3/m. Time series of dune volume change show that at our study site the foredune accretes throughout the year at similar rates (10 $m^3/m/year$), while marine erosion is obviously confined to storm surges. Foredune accretion and erosion vary spatially, which can, in part, be related to variations in beach width.

Keywords: mobile laser scanning; foredune; beach width; dune erosion; foredune recovery

1. Introduction

High-energy dissipative beaches are fringed by high (10–30 m) dunes [1,2], which act as a natural barrier against marine flooding of nearby low-lying urbanized coastal areas. Additionally, coastal foredunes provide important habitats and offer many recreational opportunities [3,4]. The foredune is the most dynamic part of the dune system as it is under influence of both marine and aeolian processes. During storm surges waves and currents erode sand from the lower parts of the foredune, resulting in scarping or slumping of the entire foredune face and hence a reduced foredune volume [5–7]. Aeolian processes increase foredune sand volume and in some cases lead to the formation of embryo dunes in front of the foredune [8]. Decades of field and laboratory research have resulted in a decent understanding of the hydrodynamical and sand transport processes resulting in foredune erosion, culminating in models that can be used in research and management projects (e.g., [9]). Similar knowledge and predictive capabilities do not yet exist for dune growth and, accordingly, full beach-dune interaction models are still in their infancy. This is, at least partly, due to a lack of high-resolution (in time and space) data sets of beach and foredune dynamics to aid

in increasing our knowledge of the mechanisms behind aeolian transport, identifying the relevant time-scales and the testing of aeolian transport models.

While a severe storm surge can result in dune erosion of O(10–100 m^3/m) along 10–100 km stretches of coast, the erosion often shows large variability on smaller scales. A difference in dune recession of 14 m for 2 cross-shore transects separated by 100 m only was observed by [10]. Moreover, an alongshore increase in dune erosion from 5 to 40 m^3/m within 200 m was found by [6]. The influence of foredune shape on dune erosion has been demonstrated to vary over spatial scales of O(10–100 m) by [11]. In the latter examples, variability in near-shore (sandbar) and beach topography resulted in variable exposure of the foredune to high waves with more dissipation and hence less dune erosion at wider beaches. Alongshore variations in beach width can potentially also result in alongshore variable dune growth as the magnitude of aeolian transport depends on, among several other factors, the distance (or fetch) over which the wind can blow over the beach. The critical fetch, i.e., the minimal fetch required to obtain maximal aeolian potential transport, varies typically between 20 and 80 m [12] and increases with wind speed and surface moisture content [13]. On narrow beaches the critical fetch is thus often not reached and, accordingly, aeolian transport is limited by the effective beach width for a given wind angle [14,15]. Adding to that, the concept of a single (critical) fetch is a simplification as wind speeds and directions often vary over the beach due to topographic steering [16]. Moreover, spatial variations in pick-up rates may result from crust formation, lag deposits and sediment sorting [17,18]. Futhermore, [19] showed that during offshore winds a secondary wind circulation, caused by topographic variations, can lead to onshore transport.

Most existing foredune studies [20–27] have used annual or less frequent data sets of topography (mainly acquired with airborne LiDAR) or data with low spatial resolutions (e.g., transects) to study relations between beach and dune topography and volume changes. However, to accurately follow changes on the scales outlined above, high resolution spatial data (1–10 m) at a high temporal resolution (monthly to seasonal) are required for extensive periods (years) in a spatially extensive (km-s) coastal stretch. The aim of this study is to investigate the use of Mobile Laser Scanning (MLS) to obtain topographic data of a beach-foredune system and to determine their usability to study changes in beach dune topography and dune volume at the indicated spatial and temporal scales. Earlier studies of coastal systems presented in [11,28,29] have demonstrated the potential of MLS for coastal monitoring. However, coastal MLS surveys have yet to be used to systematically study changes over a long period of time with high temporal resolution. We use a 2.5 year data set of repeat MLS measurements of a 25-m high foredune near Egmond aan Zee, the Netherlands. After a brief introduction of the study site, the data collection is described (Section 2). Subsequently, an assessment of the data quality is performed (Section 3). This is then followed by an analysis of the alongshore variability in foredune dynamics and post-storm foredune recovery, with a special focus on recovery of the lowest part of the foredune (Section 4). We discuss various methodological issues and the results in Section 5, and state our main findings in Section 6.

2. Materials and Methods

2.1. Field Location

The study site is a 3500 m long section of the ~120 km beach-dune system of the Dutch Holland coast between Castricum aan Zee and Egmond aan Zee (see Figure 1). The fully established foredune is ~25 m high and is partially covered with European Marram grass (*Ammophila arenaria* L.). The beach has a typical slope of ~1:30 and contains 1 or 2 intertidal slipface bars (e.g., [30]). Beach width typically varies from 140 m during low water to 50 m during high water, but temporal and spatial variations can be substantial [30]. There are no buildings on the beach except for a 50-m high video tower used for coastal monitoring (e.g., [31]). The area is often frequented by people leaving footsteps and tire tracks (bikes and cars; car admission is limited) in the sand.

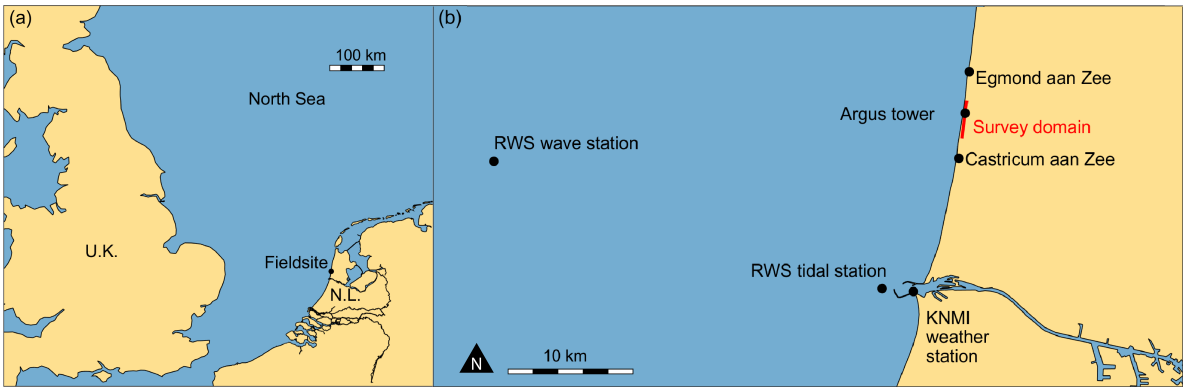

Figure 1. (**a**) Location of the field site with respect to the North Sea basin. (**b**) Location of the survey area, with locations of the Argus Tower (0 point in the local coordinate system), weather station, tidal station and wave station indicated.

The study area is microtidal with a tidal range varying between 1.2 and 1.8 m. Strong winds can substantially influence local water levels. The local wind climate was determined from hourly wind measurements from a weather station operated by the Royal Netherlands Meteorological Institute KNMI. This station is located approximately 15-km to the south of the study area. The wind climate is dominated by southwesterly winds (Figure 2) and are thus strongly onshore-oblique. Strong (>12m/s) southwesterly winds have little effect on the local water levels. In contrast, the less frequently but strong northwesterly winds lead to surges exceeding 1 m and are, due to the large fetch for this direction, often accompanied by high (>5 m) waves. These are the conditions under which the foredune can erode. The beach comprises quartz sands with a median grainsize D50 of 240 µm (i.e., fine sand).

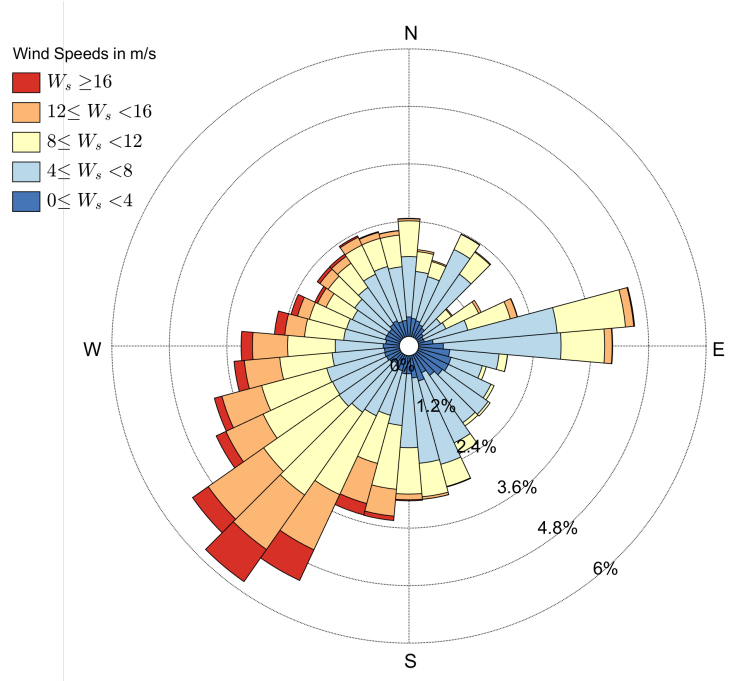

Figure 2. Wind rose from the IJmuiden weather station maintained by the Royal Netherlands Meteorological Institute KNMI (2011–2016). The station is located approximately 15 km to the south of the field site. A relatively large portion of easterly winds falls within the 80 and 90° bins. This is possibly caused by local tunneling of wind through the east-west oriented Noordzeekanaal (located to the east of the wind station). At other weather stations along the Dutch coast easterly winds are more spread out over all easterly directions.

2.2. System and Data Collection

The MLS surveys were conducted with a Riegl VZ-400 terrestrial laser scanner (TLS) combined with an OxTS RT3003 Inertial and GPS Navigation System (INS-GPS) mounted on a 4WD car (Figure 3). The laser scanner consists of a time-of-flight laser rangefinder, a vertical deflection unit and a horizontal positioning unit. The range finder measures distance to an object by transmitting a short pulse of infrared (1550 nm) light, and receiving the reflected signal. The time delay between transmission and reception is then converted to distance (accuracy 5 mm according to the manufacturer). By adding a vertical deflection unit, consisting of a fast rotating multi facet mirror, a line can be scanned instead of a single point. Furthermore, the system can be rotated in the horizontal plane. Both vertical and horizontal angles are measured with high precision (0.0005°) for each laser pulse. Combining the measured distance with the horizontal and vertical angle yields a 3D point position in the reference frame of the instrument. To convert these positions into real world coordinates, the position and orientation of the laser scanner needs to be determined. This information needs to be updated constantly as the MLS system is in motion.

Figure 3. The car mounted MLS system with INS-GPS. The photo, taken during the Dec13 survey, also shows the eroded foredune in the back.

The OxTS INS-GPS uses a combination of inertial positioning and kinematic L1/L2 GPS measurements to determine position and orientation with an update rate of 100 Hz. The system uses a dual GPS receiver setup to improve low-velocity heading accuracy. The antennas are mounted over the laser scanner, with a fixed separation of 2.0 m in the driving direction of the vehicle. spatially interpolated RTK-correction data is provided over 2G/3G mobile internet by a commercial service provider, 06-GPS.nl. The INS-GPS unit logs raw and real-time processed data. During the survey the real time position and orientation is shared with the laser scanner and linked to the observations. To achieve the highest accuracy possible, raw data can be post-processed in combined forward and backward mode. Using this method, position, heading and pitch/roll can, according to the manufacturer, be determined with an accuracy of 0.01 m, 0.1° and 0.03°, respectively. During some surveys the mobile internet connection worked intermittently, resulting in gaps in the correction data. For these surveys, correction data were obtained afterwards from the service provider. From January 2016 onward we also logged correction data for the field site ourselves at the office, using a software NTRIP client. In this way a static virtual reference station in the centre of the survey site was created. In post-processing, we replaced the GPS correction data retrieved by the navigation system with the separately obtained correction data.

During the surveys measurements were performed perpendicular to the driving direction of the car between 45° below and 28° above the horizontal with a vertical angular step size of 0.0365°. This set-up results in 2000 emitted pulses per line at a rate of 42 lines/s. With an average survey driving velocity of 4.2 m/s the distance between subsequent lines is 0.1 m. The distance between subsequent points within a line increases with increasing distance from the survey vehicle. At the survey height of 2.4 m, point distances increase from 0.005 m at 3.6 m from the scanner, to 0.67 m at 50 m on a flat horizontal surface. Each survey consisted of two alongshore passes, one with the laser scanner directed at the dune and the other pass with the laser scanner directed at the sea. The driving paths of both passes are chosen such that the two resulting point clouds overlap. In total, 13 surveys were performed between December 2013 and April 2016 (Table 1). Here we adopt an MmmYY scheme to refer to a specific survey. For example, the first survey will henceforth be termed the Dec13 survey. Alphabetic letters are added to differentiate between multiple surveys performed in a single month. We aimed to perform the seaward survey near peak low water; however, on some days due to weather conditions and daylight restrictions we were unable to do so. To test robustness 2 surveys were performed on 10-12-2013, point clouds of these two surveys (Dec13a and Dec13b) were combined to form Dec13.

Table 1. MLS survey information.

Survey	Date	nr of Points	Points per m^2	Comments
Dec13	10-12-2013	636×10^6	964	combines points from Dec13a and Dec13b
Dec13a	10-12-2013	329×10^6	629	
Dec13b	10-12-2013	307×10^6	626	driving path close to foredune
Mar14	17-03-2014	356×10^6	746	Southern part is missing
Okt14	10-10-2014	355×10^6	1238	
Jan15	16-01-2015	32×10^6	162	Additional RTK-correction data obtained
Apr15	17-04-2015	210×10^6	402	Additional RTK-correction data obtained
Jun15	29-06-2015	298×10^6	613	
Sep15	29-09-2015	337×10^6	513	Additional RTK-correction data obtained
Okt15a	09-10-2015	248×10^6	524	
Okt15b	29-10-2015	361×10^6	795	
Dec15	14-12-2015	384×10^6	431	
Jan16	25-01-2016	359×10^6	391	Additional RTK-correction data logged
Feb16	29-02-2016	372×10^6	421	Additional RTK-correction data logged
Apr16	18-04-2016	289×10^6	336	Additional RTK-correction data logged

At the end of a survey the RIEGL-VZ400 has gathered a GPS timestamped 3D point cloud in the reference frame of the instrument for each pass. In the INS-GPS raw data of the two GPS receivers, the GPS correction data as well as readings from the inertial motion sensors are available. Multiple software packages were used to process the MLS data into a digital elevation model (DEM). The adopted workflow is outlined in Appendix A. In short, outliers, vegetation, objects and surface noise were filtered from the point cloud using filters based on point density and distance from an iteratively fitted terrain model. The output of this workflow is a Digital Elevation Model (DEM) on a 1×1 m grid, with local cross-shore x positive in the seaward direction and alongshore y to the south, respectively. Elevation z is with respect to Mean Sea Level (MSL) and is positive upward. The grid size of the DEM was chosen such to allow for comparison with airborne LiDAR data (ALS) which is available for the area at a typical point density of 3 to 5 points per m^2.

3. Error Analysis

3.1. Validation

An assessment on the accuracy in z was performed for the Apr15 survey using points collected with a Trimble R8-4 RTK-GPS, which have, according to the manufacturer, an approximate horizontal

accuracy of 0.01 m and a vertical accuracy of 0.02 m. In total 914 survey points were taken in 36 cross-shore transects on the beach and the lower part of the foredune in the northern part of the survey area, between $y = -900$ and 0 m. Due to the steep slope of the foredune it was impossible to take survey points higher up the slope. In the area where the survey points were collected no vegetation was present. For each survey point the elevation of the most nearby terrain point in the filtered MLS point cloud was extracted. Points for which the closest point was found within 0.05 m in the horizontal plane were used (395 points).

Figure 4a shows the RTK-GPS and MLS survey points agree well (r^2 = 0.99) over the whole range of elevations with small differences (<0.022 m). The root-mean-square difference (RMSD) between RTK-GPS and MLS increased from 0.03 m close to the car to 0.08 m at 70 m away, which is on the lower part of the foredune (Figure 4b). This increase may reflect the expected effect of inaccuracies in pitch, roll and yaw on elevation further away from the scanner. Overall, the z-accuracy is in line with theoretical calculations based on [32], which indicate that the RMSD should be below 0.09 m at 70 m away from the car. These calculations were performed here using position and angular accuracies of both the IMU and TLS as supplied by the manufacturers (Section 2.2). Additionally, an error of 0.02 m in the position offset between the IMU and TLS and boresight angle errors of 0.004° for heading and 0.001° for pitch and roll were used, following Glennie [32]. Based on these observations and the calculations we expect the RMSD in z to increase to 0.11 m at 100 m from the car.

To study the spatial variation in MLS accuracy, the generated DEM for Feb16 was compared to a DEM generated using airborne LiDAR data (ALS) gathered on March 23 2016, referred to as LMar16 and also on a 1 × 1 m grid. The workflow to process the ALS data is very similar to the method used here to process MLS data and is fully described in [33]. Figure 4c shows that the MLS and ALS DEMs agree well (r^2 = 0.99) over the whole range of elevations with a small systematic deviation of 0.03 m and an average RMSD of 0.21 m. Positive differences values indicate that MLS observations are larger than the ALS observations. The variation in both the difference and RMSD with elevation is shown in Figure 4d. Results show that up to an elevation of 14 m the difference varies between −0.06 m and 0.06 m and the RMSD is typically 0.15 m. The small differences and its variation around zero up to up to 14 m elevation indicate that there is no offset between MLS and ALS generated DEMs. Above 15 m the RMSD increases to over 0.2 m and the difference shows an increasing trend.

3.2. Robustness

The robustness of MLS surveys was investigated by comparing two subsequent data collections performed during the Dec13 survey (Dec13a and Dec13b) and by comparing the surveys of Sep15 and Oct15a, between which aeolian and marine processes are unlikely to have affected the upper beach and foredune because of low waves and mild (off-shore directed) winds. For the Dec13 survey the first collection was performed using the standard driving path at a typical distance of 40 m from the foredune, during the second survey the driving path was more close to the foredune (20–30 m away from the foredune). Figure 4e illustrates that the MLS data are highly robust ($r^2 > 0.99$). The difference between Dec13a and Dec13b is small (<0.025 m) but negative (except for an elevation of 0). Up to a height of 11 m and RMSD remains below 0.1 m up until an elevation of 15 m. Above 15 m the RMSD increases substantially with elevation, which is mainly the result of an increasing negative difference. A driving path close to the dune causes areas with high elevation to be scanned under steeper angles, which causes the terrain to be less visible. Less terrain points reduces the ability of the off-terrain filters (Appendix A) to effectively filter off-terrain points, resulting in a higher elevation. Already under the normal driving path for some cross-shore transects we were unable to capture points above 13.8 m. Due to the lack of data for some cross-shore transects above this elevation we chose the 13 m contour instead of the 15 m contour as the upper limit for our volume analysis, as described in the next section.

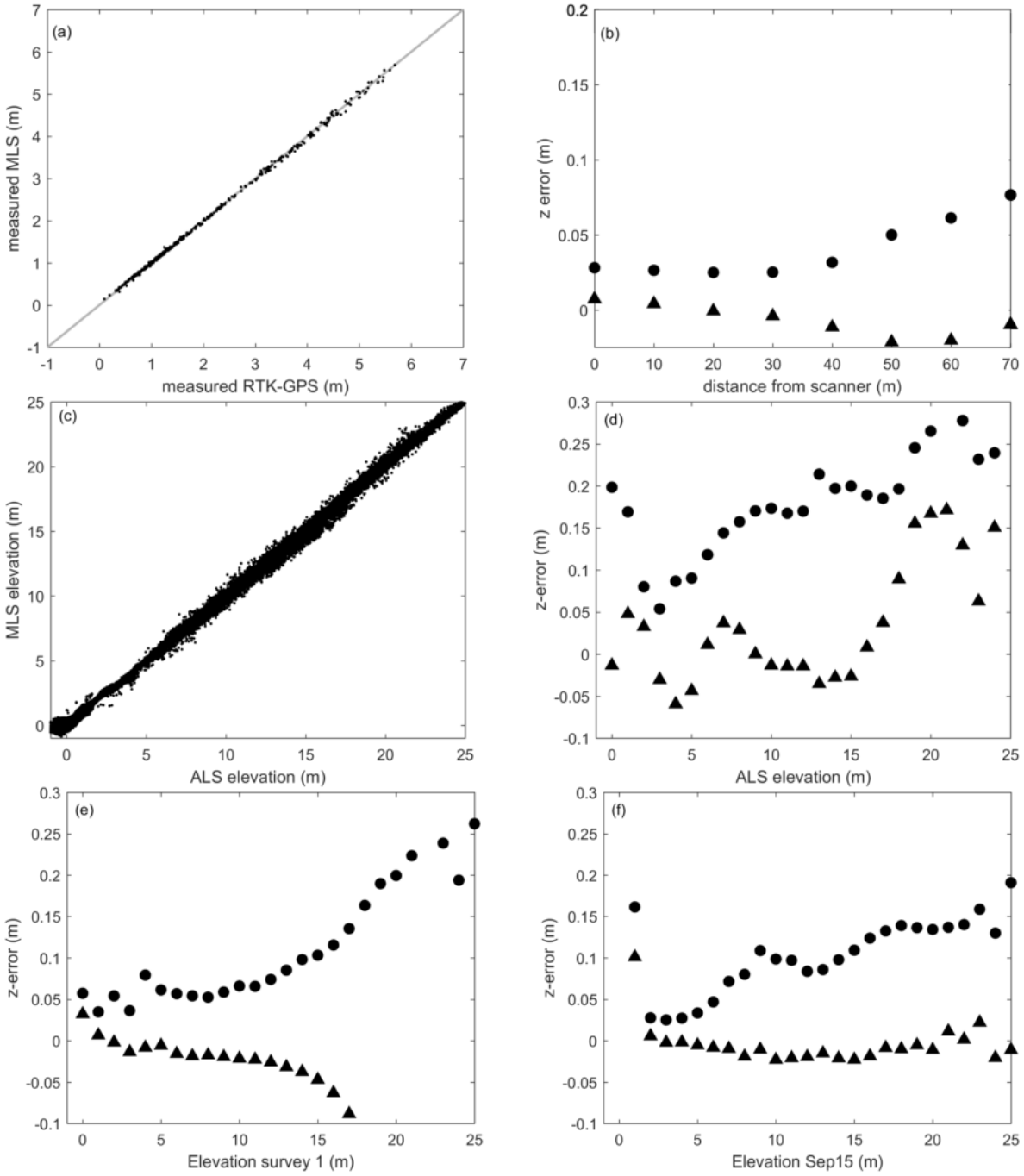

Figure 4. (**a**) Measured MLS versus RTK-GPS elevation. The grey line is the line of equality; (**b**) The average (black triangles) and root-mean-square difference (black dots) between MLS and RTK-GPS elevation taken over 10-m wide bins; (**c**) ALS (LMAR16) versus MLS DEM (Feb16) gridpoints. The grey line is the line of equality; (**c**) The average (black triangles) and root-mean-square difference (black dots) between ALS DEM and MLS DEM taken as a function of elevation; (**e**) Same as (**d**) but than for the two surveys of Dec13; (**f**) same as (**d**) but than for the Sep15 and Oct15a surveys.

4. Beach-Dune Dynamics

4.1. Methods

The DEMs were analysed to study spatial and temporal change in beach and dune topography. The cross-shore boundaries of our study domain were chosen based on data availability, in all scans and for all cross-shore transects the lowest available contour line (X_1) was the +1 m contour and the

highest (X_{13}) was the +13 m contour line (based on data availability). The contour for the dunefoot (X_{DF}), which splits the beach from the foredune, was set at $z = 3$ m. For each cross-shore transect the most offshore point for which $z = 1$ m (X_1) and the most duneward points for which and $z = 13$ m (X_{13}) were extracted.

The method for deriving the dune volume change and dune slope is outlined in Figure 5. Dune volume V was calculated by integration of the elevation between the X_{DF} and X_{13} points. The elevation of the lower bound (X_{DF}) was subtracted prior to integration. As both contour lines shift over time the volume was calculated with respect to a reference point (X_{ref}) located deeper inside the dune. This yields:

$$V = \int_{X_{13}}^{X_{DF}} (z - 3)\delta x + \int_{X_{ref}}^{X_{13}} (13 - 3)\delta x, \quad (1)$$

Subsequently, the beach width W, defined as the distance between the X_{DF} and 1 m contour line (X_1), was calculated for each transect.

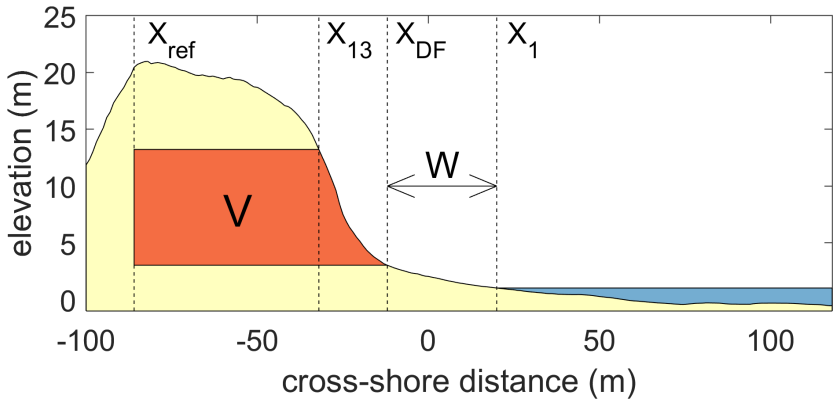

Figure 5. Definitions used for the analysis. Positions of the landward boundary (X_{ref}), 10 m elevation contour (X_{13}), the dune foot (X_{DF}) and the 1 m elevation contour (X_1). These positions are used to calculate dune volume (V) and beach width (W). Cross-section shown is located at alongshore coordinate 1100 m in later figures.

The accuracy of the foredune volume was investigated using the DEMs of surveys used for the MLS intercomparison presented in Section 3 (Sep15 and Oct15a). For all transects in both DEMs foredune volumes were determined. The RMS difference in foredune volume over all transects was 0.25 m^3/m. This value gives a good estimate of the uncertainty in foredune volume when comparing MLS surveys.

4.2. Conditions

Figure 6 illustrates hourly wind speed and maximum water level at the coast including the effects of set-up and run-up through implementation of the Stockdon parametrizations [34] as described in [35]. Both wave height and length needed to calculate set-up and run-up as well as offshore water levels were measured outside the harbor of IJmuiden some 15 km south of the study site. Wind speeds peak during the winter months. As aforementioned, strong north-westerlies results in a storm surge along the Dutch coast. The first storm surge (reaching above 4 m MSL) in Figure 6b is associated with a storm on 5 December 2013, just before the Dec13 survey [36]. During the monitoring period 2 additional storms in the autumn-winter of 2014–2015 resulted in substantial surges. A minor surge also occurred in November 2015. Other peaks in wind speed are related to winds from the south-west; these did not result in any appreciable surge.

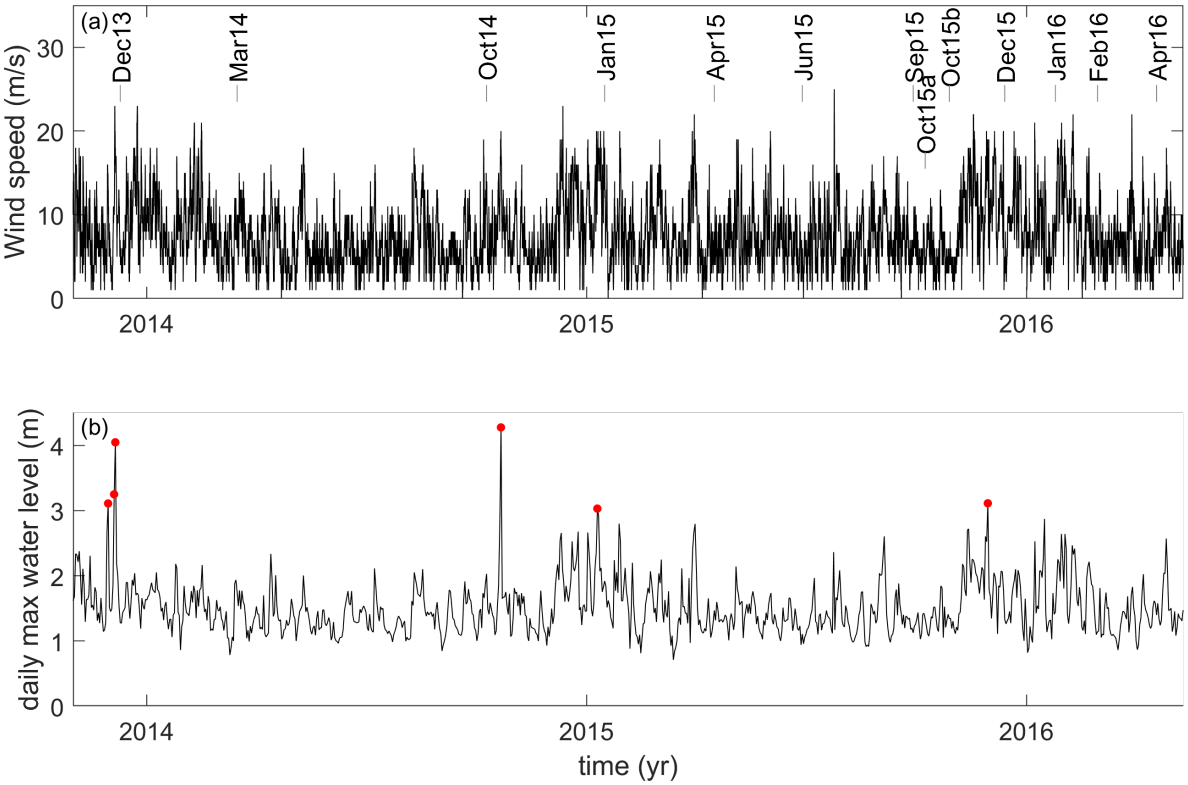

Figure 6. Environmental conditions during the measurement period. (**a**) shows the absolute wind speed; scan dates are indicated; (**b**) shows the maximum daily water level including the effects of set-up and run-up. Days where water levels reached above the height of the dune foot (+3 m) are marked with red dots.

4.3. Topographic Changes

The topography obtained during the Dec13 survey, the start of the observation period, is shown in Figure 7a. As aforementioned, the beach-dune system was subjected to a storm surge a few days before this survey and the foredune was eroded substantially. The majority of the sand eroded from the dune was, as is common during such events [37,38], deposited on the beach, which resulted in a relatively wide beach and steep foredune (see in the background of Figure 3), similar to that observed after earlier erosion events at Egmond [6]. In some cross-shore transects the MLS was able to scan the entire foredune (up to its full height of around 25 m) while for other cross-shore transects the upper part of the foredune (13.8 m was the highest available elevation for one transect) was not in the line of sight of the scanner.

The topographic change over the entire monitoring period, between the Dec13 and Apr16 surveys varied substantially alongshore (Figure 7b). To study spatio-temporal variations in dune volume, the study site was split into seven alongshore zones selected to maximize differentiation between accretion and erosion zones. All cross-shore transects in the accretion zones have net acretion over the whole period, after a 10 m averaging window to remove small scale noise. The opposite is the case for the erosion zones. The most southern and most northern parts are excluded from the zones as beach restaurants that are located there during summer; their placement often involves substantial sand-moving activities. Odd-numbered zones accreted over the study period while in all even-numbered zones erosion prevailed landward of the initial 3-m contour line (Figure 8a). Zones 2 and 6 also suffered major losses high up (above the 9 m contour) in the foredune, while in zone 4 the lower part of the foredune lost most sand. In 6 out of the 7 zones the beach accreted below the initial 3-m; only in zone 4 the 3-m contour moved landward. The elevation decrease was largest in zone 2, where elevation decreases of over 2 m were observed at the higher parts (above the 9 m contour) of the foredune slope. In zone 3 the largest increases in height were observed, nearly 2 m in some

places. The beach width W, shown in Figure 8b, varied substantially throughout the measurement period at all cross-shore locations, as expressed by the on average 14-m wide bands of $W \pm 1$ standard deviation. However, the beach was on average wider in the north than in the south of the study site. The acretion zones were generally wider than the erosion zones. The largest reduction in elevation was observed in an erosion zone where both the upper beach was dynamic and the beach was more narrow. Moreover, in these areas the seaward progression of the dune foot was smaller. In the parts with the largest volume gains, the beach was wider and the upper beach was less dynamic, while the dune foot progressed in the seaward direction.

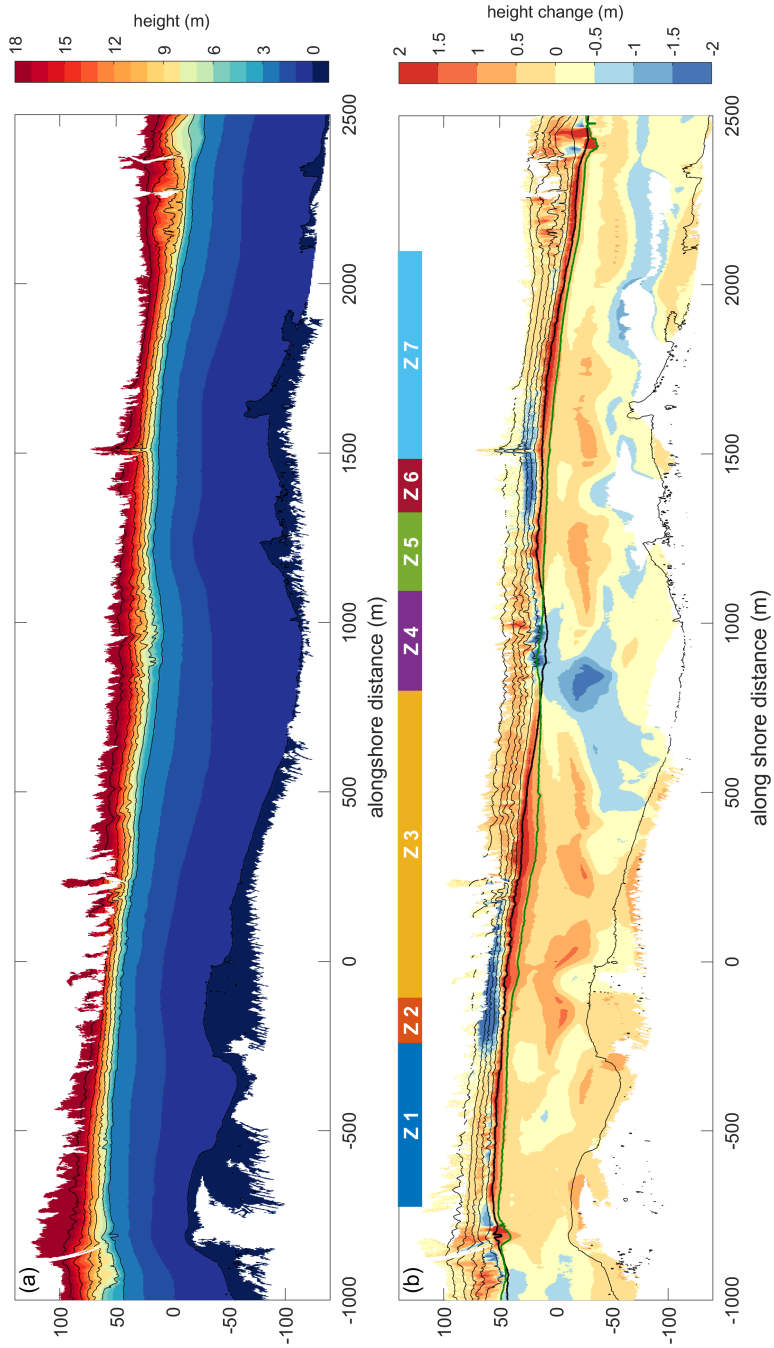

Figure 7. Measured topography in the survey area. (**a**) shows the topography for 14-12-2012; (**b**) shows the change in topography. The thin black lines are bed-elevation contours from the Dec13 survey, starting at MSL with a 3-m interval. The +3 m contour for the Dec13 survey is shown as a thick black line and the location of the 3-m contour in the Apr16 survey is shown with a thick green line.

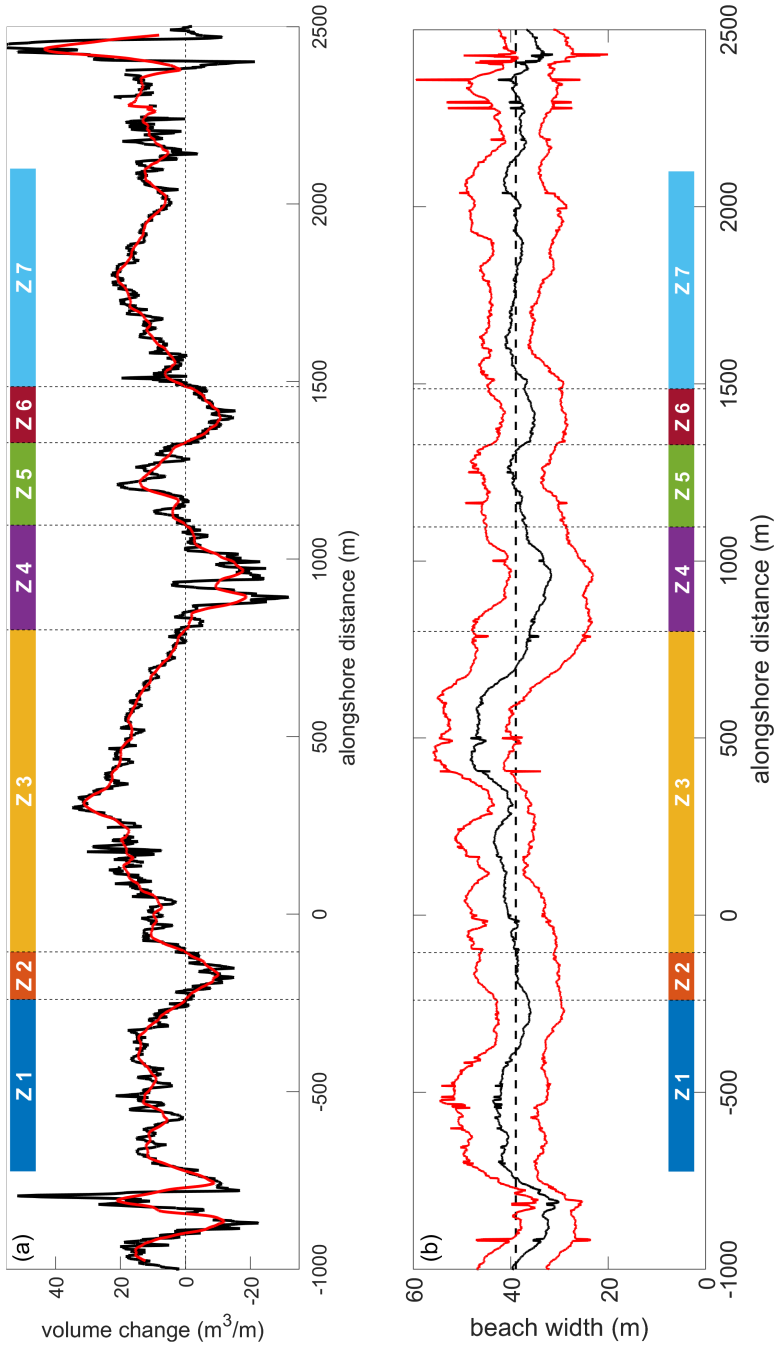

Figure 8. Volume change and beach width. (**a**) shows the alongshore variation in volume change between survey Dec13 and Apr15 (black line) with the alongshore volume changes after applying a 50-m averaging window (red line); (**b**) shows the average beach width over all surveys (black line) together with ±1 standard deviation (red lines). The dashed line is the alongshore average beach width for zones 1 to 7. The Mar14 was excluded because of missing data.

4.4. Spatio-Temporal Variation in Dune Volume Change

The evolution of dune volume change (Figure 9a) also shows the clustering of our study site in erosive zones (# 2, 4 and 6) with red tinted markers (orange, purple and red) and net accretive (# 1, 3, 5 and 7) zones with other markers (blue, yellow, green and light blue). The clustering resulted primarily from the strong variability in dune erosion in the 2014–2015 winter. The erosion was smallest (7.4 m^3/m) in zone 3 and largest in zone 2 (30.3 m^3/m). Zone 4 was the only zone to erode (3.2 m^3/m) during the minor surge in November 2015. The 4 accretive zones differed in the rate of accretion,

which is especially visible for 2015. For example, zone 3 accreted by 12.3 m^3/m between Jan15 and Dec15, while the increase was only 4.6 m^3/m in zone 5. Similar variability in accretion can also be seen for 2014, albeit less pronounced. Figure 9b illustrates the temporal variability in average beach width in the 7 zones. The zones that eroded most in winter 2014–2015 (# 2 and 6) and in winter 2015–2016 (zone 4) had had the narrowest, 20 to 30 m, pre-storm beach widths (W). This shows that also for this location, pre-storm beach width has a strong control on dune erosion volumes. A relationship between beach width and accretion is not immediately obvious.

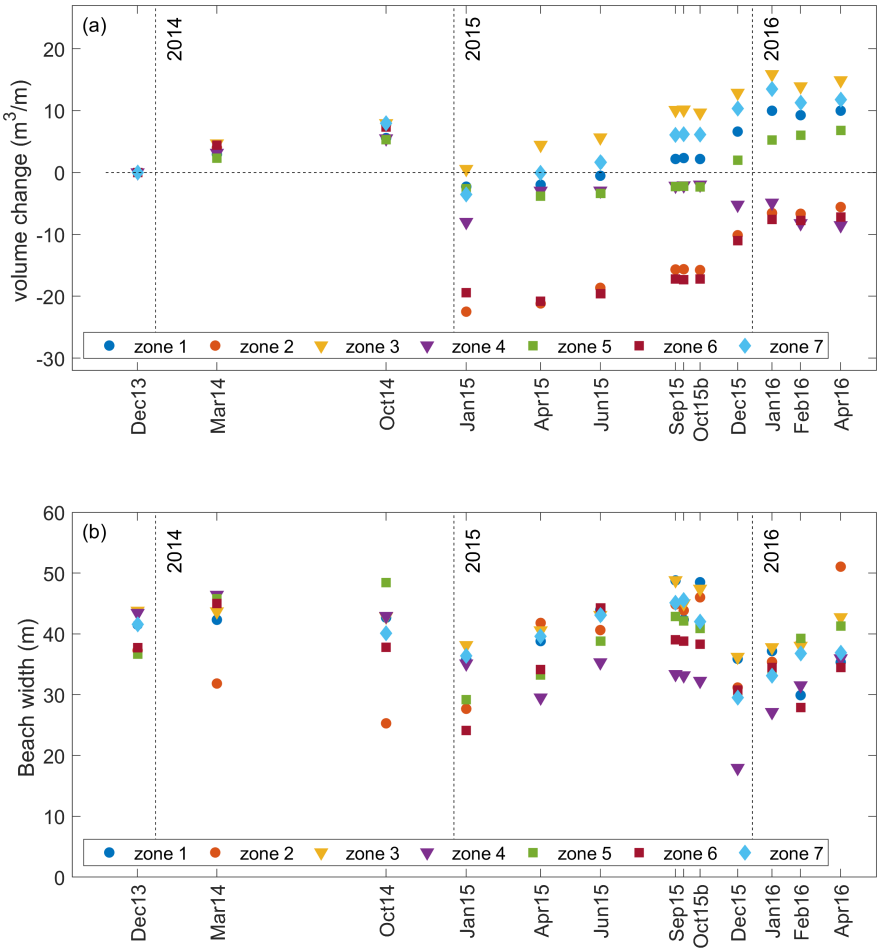

Figure 9. (**a**) Dune volume change throughout the measurement period with respect to the initial dune volume. Colored dots show dune volume for the zones defined in Section 4.3; (**b**) the beach width for each zone (between 1 m and 3 m contour lines) throughout the measurement period.

To explore the difference in recovery after the erosion events of the 2013–2014 and 2014–2015 winters we examine the volume changes of the lower part (from 3 to 5 m) of the foredune in more detail. This is the part of the foredune where most dynamics occur and where recovery, in the form of embryo dune formation, starts. Recovery of the lower part of the foredune is, as shown in Figure 10a, rapid (<3 months) and alongshore uniform after the 2013–2014 winter period. Erosion for the 2014–2015 winter period resulted only in erosion locally (around alongshore coordinates −300 and 1500 m). Fo this period recovery of the lower parts of the foredune did not occur alongshore uniform but started at alongshore coordinates 1600 m and 0 m and then spread to the north up to alongshore coordinates 1300 m and −300 m (see Figure 10b). Recovery time for this period was much longer and the most northern part of the eroded area had only recovered just before the 2015–2016 winter period. For both periods the beach width, shown in Figure 10c, at the start of the recovery period was very different. In the Dec13 survey the average width of the upper beach varied between 40 and 60 m while

in the Jan14 survey beach width varied between 25 and 40 meters. For the latter period the smallest beach widths coincide with the eroded areas.

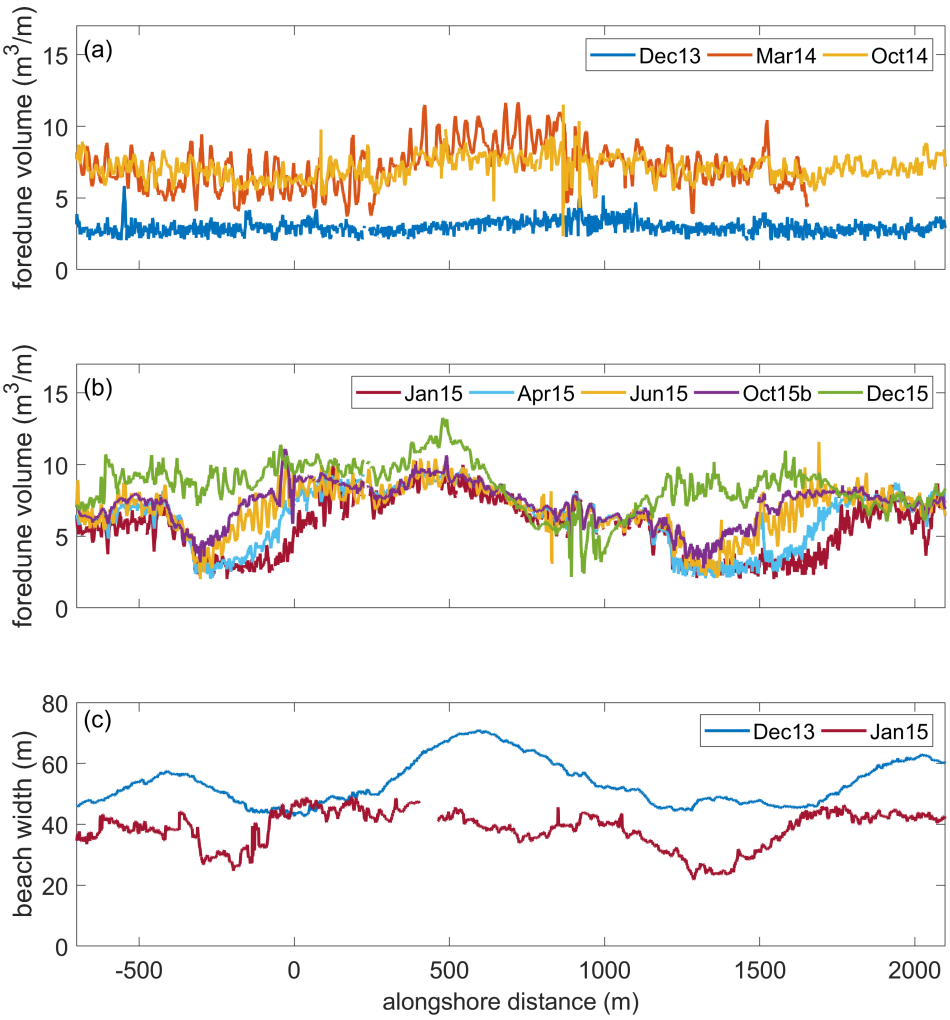

Figure 10. (**a**) Volume between the 3 and 5 m contour line as a function of the alongshore coordinate for the Dec13, Mar14 and Oct14 surveys (**b**) same as (**a**) but then for Jan15, Apr15, Jun15, Oct15b and Dec15 surveys, (**c**) width of the upper beach for Dec13 and Jan15 surveys.

To examine the dependence of dune volume change on beach width in more detail, we computed ΔV between Dec13 and Apr16 in 10 m wide alongshore bins and compared it to the time-averaged beach width in the same bins. Figure 11a displays that the binned ΔV and W are positively related with a slope of 3.2 m^3/m^2. The correlation coefficient squared (r^2) of the best-fit linear line is 0.48. Average beach widths less than 35 m resulted in net erosion, while wider beaches net accreted. This overall response appears to be a combined effects of larger volume losses and smaller gains on narrower beaches, and smaller losses and larger gains on wider beaches. This is illustrated further in Figure 11b,c, which show positive dependencies of dune volume change on beach width during the erosional Oct14–Apr15 period and accretional Apr14–Sep14 period. For these two periods the intertidal beach width at the start of the period was taken. The dependence for dune erosion is stronger (slope of best-fit line is 0.65 m^3/m^2 vs. 0.32 m^3/m^2) while the scatter is similar (r^2 = 0.44 vs. 0.43).

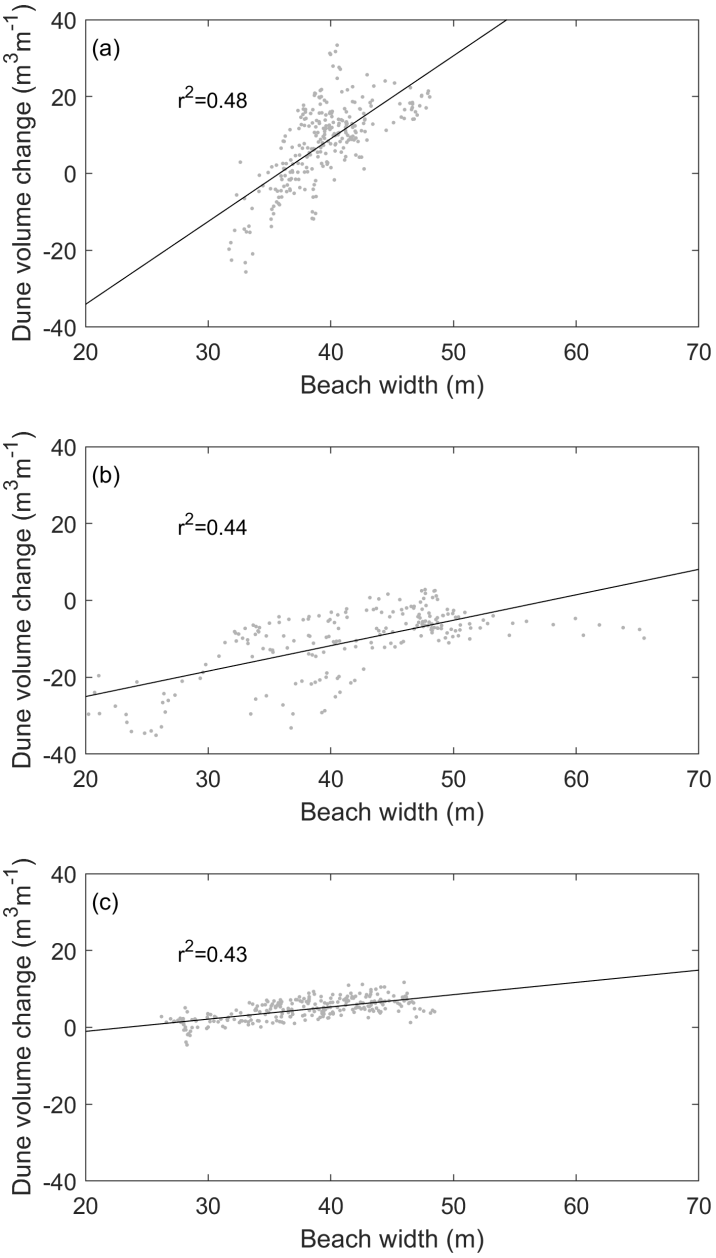

Figure 11. (**a**) total volume change as a function of average beach width (grey points) of 10-m alongshore bins; (**b**) total volume change as a function of beach width at the start of the period for the erosive period Oct14 and Apr15; (**c**) same as (**b**) but for the accretion dominated period Apr15 to and Sep15. Black lines are the best fit linear lines, all of which are statistically significant at the 95% confidence level.

5. Discussion

5.1. Methodological Issues

Our results show that the present set-up MLS can be used to study the dynamics of the lower 15 m of the beach-foredune system at Egmond. While ground truthing of the MLS data with RTK survey points confirms that the observations are generally well within the expected range, there are several methodological issues that need to be considered when interpreting MLS data. Shadow effects occur when vegetation, an object or a part of the terrain blocks the view of the laser towards a surface point. This may, given our survey set-up, be the case landward of embryo dunes found near the dune foot and higher up the dune where vegetation density increases and the dune slope decreases. Consequently, in grid cells that are completely hidden from sight by the laser, no points can be gathered. Here,

we estimated the surface height by interpolation. Partly hidden cells often contain the highest points only, resulting in an overestimation of the average grid height. The terrain filters (Appendix A) are also affected by point shadowing as they require sufficient terrain points as a base to detect outliers. Especially higher up on the foredune the laser beam may hit vegetation points within a certain grid cell only. Consequently the lower vegetation points will be chosen as base points for the filters resulting in wrong elevation estimates [39]. While we were unable to check this, we do not expect this to be a major issue below the 10 m contour as there vegetation is scarce. Moreover, only single return points were used for grid generation. In vegetation, the small branches and stems often lead to multiple returns. Our system is only able to detect multiple returns if the reflections are more than 1 m apart. In the present workflow if the amount of ground points is over 1% per 0.25 m^2 the filters are able to differentiate between vegetation and the terrain. Potentially, the use of the full waveform of the returned laser signal allows for more sophisticated methods to differentiate between vegetation and terrain (see [28,40]). While the MLS-ALS comparison showed good correspondence up to $z = 15$ m, at our site, shadowing effects limited our analysis of volume change to the lowest 13 m of the foredune.

5.2. Dune Dynamics

During accretion periods the dune volume increased with a typical rate of 14.8 $m^3/m/yr$ at our site while during the winter of 2014–2015 some sections lost over 20 m^3/m. Overall, this resulted in net increase of 10.1 ± 8.6 m^3/m over the entire observation period. The foredune accreted throughout the year, and for 2015 the increase was nearly linear in time from spring to autumn. Spatial variation in dune volume change was especially strong for erosion, and the largest differences between the studied zones thus result from erosion events. These growth and erosion rates are in line with previously reported long term volume changes for the Dutch Holland coast which are based on annual observations along 250 m spaced cross-shore transects [41].

Alongshore variability in both negative and positive volume change correlated positively with beach width. For foredune erosion this confirms earlier observations and model simulations for the Dutch coast [6,41,42], and observations elsewhere [21,23,43]. During a storm period we found that the amount of erosion decreased if the local beach was wider at a rate of 0.66 m^3/m per m beach width. During calmer periods we observed for each extra meter of beach width 0.32 m^3/m more accretion. While a positive relation between beach width and growth was established previously at macro scale O(1 km) and up [1,44] the usage of high (spatial and temporal) resolution MLS observations allowed us to be first to establish this relation at small scales O(10–100 m). Local beach width is likely to be a proxy for the locally available sand. Such relations explain the differences in recovery period between the winters of 2013–2014 (wide beach) winter and the 2014–2015 (narrow beach). Similarly, the differences in post-storm beach width for zones 3 (wide) and 5 (narrow) after the winter of 2014–2015 lead to differences in recovery (see Figure 9). Both these observations suggest that how sediments are redistributed in the nearshore zone during an erosion event affects the post-storm aeolian sediment availability. These volume increases are caused by a combination of aeolian transport events from shore normal, oblique and nearly shore parallel angles. This is further substantiated by spatial variation in the recovery of the lower part of the foredune as recovery of the northern parts lags with respect to the southern parts. This indicates that the area southward of the transect, including the foredune area itself, may have acted as the sediment source. This is in line with the dominant SW wind direction (Figure 2) and suggest that for these wind conditions the northern parts of erosion hotspots recover the slowest. Additional erosion events should be analyzed to confirm this. In our analysis the intertidal part of the beach is missing which may have affected our analyses if the intertidal zone is an important source for wind-blown sand (e.g., [45]). Sediment input through secondary wind flows such as those identified by [19] for offshore winds are likely small as those conditions are rare and the associated wind velocities are small. Potentially the relationship between volume gain and beach width can be improved by using the fetch of the wind rather than cross-shore beach width, especially given the strong onshore-oblique character of the wind and alongshore variability in beach

width. However, while estimates of critical fetch exist [46,47], determining the actual fetch is complex. Onshore wind flows are affected by the presence of the foredune causing a local variations in wind direction and speed [16] which influence fetch and sediment pick-up rates, respectively. In addition, surface moisture dynamics limit the amounts of sediments available for aeolian transport from the intertidal beach either by preventing sediment pick-up or reducing pick-up rates [13]. Further work, including modeling aeolian of sediment transport the beach on daily to yearly scales (e.g., [47]) is necessary to elucidate the role of beach morphology on alongshore variable dune growth and recovery. We believe that our data can serve to design and validate such models. Moreover, we hope that our data set contributes to further understanding of the processes/mechanisms behind aeolian transport in coastal environments.

6. Conclusions

In this paper, the applicability of Mobile Laser Scanning to study changes in foredune topography and volume was investigated. Using a car-mounted MLS system with attached inertial navigation system beach and dune topography along a 3.5-km beach stretch of the Dutch coast was recorded 13 times during a 2-year period. Robustness and repeatability tests indicated that the RMS differences are typically 0.1 m while dune volume can be determined with an accuracy of 0.25 m^3m^{-1} between the +3 and +10 m contour lines. This upper limit is related to the dense cover of marram grass, which prohibits the MLS to see the ground. The data show that beach width controls alongshore variability in both dune erosion and accretion. In our data, in which beach width varied between 20 to 70 m, a 1-m wider beach resulted in about 0.66 m^3/m less erosion during storms events and 0.32 m^3/m more accretion during calm conditions.

Author Contributions: Conceptualization, G.R. and J.D.; methodology, J.D. and M.v.M.; software, J.D.; validation, J.D. and G.R.; formal analysis, J.D.; investigation, M.v.M. and J.D.; resources, M.v.M. and G.R.; data curation, J.D. and M.v.M.; writing—original draft preparation, J.D.; writing—review and editing, G.R. and M.v.M.; visualization, J.D.; supervision, G.R.; project administration, G.R.; funding acquisition, G.R.

Funding: This research was supported by the Dutch Technology Foundation STW (Vici project 13709 to Gerben Ruessink), which is part of the Netherlands Organisation for Scientific Research (NWO), and which is partly funded by the Ministry of Economic affairs.

Acknowledgments: We thank Henk Markies for his excellent support in performing the MLS measurements and Pam Hage, Winnie de Winter and Yvonne Smit for their assistance with the RTK-GPS measurements.

Conflicts of Interest: The authors declare no conflict of interest. The founding sponsors had no role in the design of the study; in the collection, analyses, or interpretation of data; in the writing of the manuscript, or in the decision to publish the results.

Appendix A. Workflow

1. The raw data gathered by the INS-GPS system and the external GPS correction data were post-processed in combined forward and backward mode using RT Post-Process software [48]. After data quality screening, a time-stamped position and orientation file was exported together with a second file containing time-stamped information on position and orientation accuracy. For the periods in which the data link with the RTK correction data service provider was lost, the post-processing procedure was slightly different. First, additional GNSS correction data was obtained in RINEX format. This correction data was also imported in the RT Post-Process software and used during the post-processing procedure.
2. In the RiPROCESS software [49], the position and orientation file was imported into the project. The post-processed position and orientation file then overwrites the realtime position and orientation data linked to each point during the survey. Navigation data is linked to laser scan data using the recorded GPS time stamps.

3. A transformation matrix containing the rotation and translation between the TLS and the INS-GPS measurement axes was applied to the position and orientation data to correct for the offset between both devices. A bore sighting procedure was performed to determine the pitch, roll and yaw offsets, needed to generate this transformation matrix, with high accuracy (details provided at the end of this Appendix).
4. A georeferenced point cloud was generated from the survey data.
5. The point cloud was filtered 4 times to classify points and to filter different types of noise. First, isolated points, defined as points with less than 5 neighboring points within a radius of 2 m, were detected. The next three filter steps were all performed using off-terrain filters, albeit used with different settings (see Table A1), for details on the working of each filter setting we refer to the help function of RiPROCESS sofware [49]. In short, the filter separates points from the underlying terrain by determining the distance of each point to an estimate of the ground surface. When the distance of a point to the estimated surface is larger than the given tolerance factor multiplied by the grid size, the point is filtered. The filter works in a hierarchic manner filtering the points at different spatial scales working from a coarse grid to the final base grid's cell size. Grid sizes at each level can be calculated by multiplying the base grid size with $2^{level-1}$, at each level the points falling outside the tolerance range are removed before continuing filtering at a lower level. At the second filter step the off-terrain filter was used with specific settings (vegetation) to delineate high vegetation and objects from terrain values. In the third step, the off-terrain point filter was applied to separate the terrain from the remaining low vegetation and other objects. In the final step, a fine filter was used to detect small-scale noise, for instance, caused by tire tracks. The filtered points were not removed but classified as isolated points [064], vegetation [003], non-terrain [001] and noise [037], respectively. The numbers indicate the classification codes. The Argus tower, and points reflected from the sea surface were classified manually as building [007] and water [009], respectively. The remaining non-classified points were classified as ground [002].
6. The obtained point clouds were cut in tiles of 512 $\times$ 512 m and exported per survey record in a .las (1.4) format using the WGS84 datum. One tile may cover multiple passes. This results in separate files per pass.
7. The tiled data was subsequently imported in Matlab® [50], and combined. Points classified as ground were extracted.
8. A single return filter was applied on the extracted ground points to remove points from observations with multiple returns.
9. The time stamp of each point was compared with the timeseries of position and orientation accuracy. Points were removed from the dataset for a 3D position error larger than 0.025 m, a heading error larger than 0.07° and a pitch/roll error larger than 0.03°.
10. The remaining points were transformed to the Dutch RD coordinate system, with the vertical reference point, called NAP (Amsterdam ordnance datum), having its zero level at Mean Sea Level. From the horizontal coordinates the location of the beach pole seaward of the Argus tower (102,572 m, 511,553 m) was subtracted, making the beach pole the local (0,0) coordinate. Subsequently, the grid was rotated by 172 degrees in clockwise direction, creating a cross—alongshore coordinate system in which the cross-shore-coordinate increases in the seaward direction and the alongshore-coordinate increases in the southward direction.
11. The shifted and rotated points were then averaged on a 1 $\times$ 1 m grid by averaging all elevation z values (in NAP) of all points within a radius of 1 m from a grid point coordinate. Additionally, the number of data points and standard deviation of the point elevation was stored per grid cell.
12. Small holes in the elevation model were replaced by means of smoothed interpolation using the values of neighbouring cells [51]. The final end products are digital models of elevation, point count and standard deviation in elevation.

Table A1. Settings for the off-terrain point filters.

	Vegetation	Terrain	Noise
Base grid's cell size	0.25 m	1 m	0.25 m
Number of Levels	8	4	4
Tolerance factor	0.7	1	0.7
Percentile	1%	1%	1%
Maximum slope angle	60°	90°	90°
Fine filter tolerance filter	0.1 m	0.1 m	0.05 m

Bore Sighting Procedure

The position and orientation of the TLS with respect to the INS-GPS is not known exactly. Any misalignment causes scanned objects or parts of the terrain to be registered to the wrong geographical coordinates. Moreover, objects scanned from multiple sides show up multiple times at different coordinates. Because the VZ-400 laser scanner has the possibility for precise control of the horizontal angle, a bore-sighting procedure can be used to accurately determine the pitch, roll and yaw offsets between the TLS and the INS-GPS measurement axes. This bore-sighting procedure needs to be repeated every time the laser scanner has been detached from the INS-GPS (e.g., for transport or service purposes).

The bore sighing procedure within the RiPROCESS software was used and is described fully in [52]. In short, multiple scans of a large facade containing many planar features under different horizontal TLS angles serve as input for the procedure. The obtained scans are processed following the workflow described above up to and including step 4; however, the used transformation matrix is a first estimate of the exact transformation matrix. On the obtained point cloud a planar surface fitting algorithm was applied on all individual scans. Planes were automatically detected (settings: minimum plane inclination angle 45°, maximum plane point deviation 0.03 m, minimal plane point count of 100). The obtained surfaces were subsequently matched between all scans (settings: search radius 0.1 m, angular tolerance 0.05° and maximal normal distance of 0.05 m) using a least square fit (setting: tolerance 0.0001 m) to maximize overlap of these surfaces. Roll, pitch and yaw angles were optimized based on the outcomes of the fitting procedure. The obtained pitch, roll and yaw angles are used to recalculate the point cloud and the bore sight alignment procedure is repeated until the obtained pitch, roll and yaw offset angles converge.

The TLS was detached from the INS-GPS between surveys Jan15 and Apr15. For surveys Dec13 through Jan15 the bore sighting survey was performed at an industrial area in Houten, The Netherlands (N 52.0225°, E 5.1483°) on 3 February 2014. During this survey, 2 sections (240 m) of 7 buildings surrounding a small lake were scanned. The second survey for bore sighting was performed near an industrial site in Nieuwegein, the Netherlands (N 52.0235°, E 5.1240°) on 15 April 2015. During that survey two sides (230 m and 115 m long) of a windowless 14-m high building were scanned. During both surveys 20 different scans were performed as each side was scanned under 10 different compass angles. Angles varied with a step size of 30 degrees; 0°(forward) and 180°(backward) were excluded.

References

1. Short, A.; Hesp, P. Wave, beach and dune interactions in southeastern Australia. *Mar. Geol.* **1982**, *48*, 259–284. [CrossRef]
2. Durán, O.; Moore, L.J. Vegetation controls on the maximum size of coastal dunes. *Proc. Natl. Acad. Sci. USA* **2013**, *110*, 17217–17222. [CrossRef] [PubMed]
3. Arens, S.M.; Wiersma, J. The Dutch foredunes: inventory and classification. *J. Coast. Res.* **1994**, *10*, 189–202.
4. Everard, M.; Jones, L.; Watts, B. Have we neglected the societal importance of sand dunes? An ecosystem services perspective. *Aquat. Conserv. Mar. Freshw. Ecosyst.* **2010**, *20*, 476–487. [CrossRef]

5. Carter, R.W.G.; Stone, G.W. Mechanisms associated with the erosion of sand dune cliffs, Magilligan, Northern Ireland. *Earth Surf. Process. Landf.* **1989**, *14*, 1–10. [CrossRef]
6. De Winter, R.C.; Gongriep, F.; Ruessink, B.G. Observations and modeling of alongshore variability in dune erosion at Egmond aan Zee, The Netherlands. *Coast. Eng.* **2015**, *99*, 167–175. [CrossRef]
7. Castelle, B.; Marieu, V.; Bujan, S.; Splinter, K.D.; Robinet, A.; Sénéchal, N.; Ferreira, S. Impact of the winter 2013–2014 series of severe Western Europe storms on a double-barred sandy coast: Beach and dune erosion and megacusp embayments. *Geomorphology* **2015**, *238*, 135–148. [CrossRef]
8. Hesp, P. Foredunes and blowouts: Initiation, geomorphology and dynamics. *Geomorphology* **2002**, *48*, 245–268. [CrossRef]
9. Roelvink, D.; Reniers, A.; van Dongeren, A.; van Thiel de Vries, J.; McCall, R.; Lescinski, J. Modelling storm impacts on beaches, dunes and barrier islands. *Coast. Eng.* **2009**, *56*, 1133–1152. [CrossRef]
10. Thornton, E.B.; MacMahan, J.; Sallenger, A. Rip currents, mega-cusps, and eroding dunes. *Mar. Geol.* **2007**, *240*, 151–167. [CrossRef]
11. Brodie, K.L.; Spore, N.J. Foredune classification and storm repsonse: Automated analysis of terrestrial LiDAR DEMS. In *The Proceedings of the Coastal Sediments 2015*; World Scientific: Singapore, 2015.
12. Davidson-Arnott, R.G.D.; Law, M.N. Measurement and prediction of long-term sediment supply to coastal foredunes. *J. Coast. Res.* **1996**, *12*, 654–663.
13. Delgado-Fernandez, I. A review of the application of the fetch effect to modelling sand supply to coastal foredunes. *Aeolian Res.* **2010**, *2*, 61–70. [CrossRef]
14. Nordstrom, K.F.; Jackson, N.L. Effect of source width and tidal elevation changes on aeolian transport on an estuarine beach. *Sedimentology* **1992**, *39*, 769–778. [CrossRef]
15. Bauer, B.O.; Davidson-Arnott, R.G. A general framework for modeling sediment supply to coastal dunes including wind angle, beach geometry, and fetch effects. *Geomorphology* **2003**, *49*, 89–108. [CrossRef]
16. Walker, I.J.; Davidson-Arnott, R.G.; Bauer, B.O.; Hesp, P.A.; Delgado-Fernandez, I.; Ollerhead, J.; Smyth, T.A. Scale-dependent perspectives on the geomorphology and evolution of beach-dune systems. *Earth-Sci. Rev.* **2017**, *171*, 220–253. [CrossRef]
17. Van der Wal, D. Effects of fetch and surface texture on aeolian sand transport on two nourished beaches. *J. Arid Environ.* **1998**, *39*, 533–547. [CrossRef]
18. De Vries, S.; de Vries, J.V.T.; van Rijn, L.; Arens, S.; Ranasinghe, R. Aeolian sediment transport in supply limited situations. *Aeolian Res.* **2014**, *12*, 75–85. [CrossRef]
19. Lynch, K.; Jackson, D.W.T.; Cooper, J.A.G. Aeolian fetch distance and secondary airflow effects: The influence of micro-scale variables on meso-scale foredune development. *Earth Surf. Process. Landf.* **2008**, *33*, 991–1005. [CrossRef]
20. Guillén, J.; Stive, M.J.F.; Capobianco, M. Shoreline evolution of the Holland coast on a decadal scale. *Earth Surf. Process. Landf.* **1999**, *24*, 517–536. [CrossRef]
21. Saye, S.; van der Wal, D.; Pye, K.; Blott, S. Beach–dune morphological relationships and erosion/accretion: An investigation at five sites in England and Wales using LIDAR data. *Geomorphology* **2005**, *72*, 128–155. [CrossRef]
22. Claudino-Sales, V.; Wang, P.; Horwitz, M.H. Factors controlling the survival of coastal dunes during multiple hurricane impacts in 2004 and 2005: Santa Rosa barrier island, Florida. *Geomorphology* **2008**, *95*, 295–315. [CrossRef]
23. Houser, C.; Hapke, C.; Hamilton, S. Controls on coastal dune morphology, shoreline erosion and barrier island response to extreme storms. *Geomorphology* **2008**, *100*, 223–240. [CrossRef]
24. Mitasova, H.; Hardin, E.; Overton, M.F.; Kurum, M.O. Geospatial analysis of vulnerable beach-foredune systems from decadal time series of lidar data. *J. Coast. Conserv.* **2010**, *14*, 161–172. [CrossRef]
25. Priestas, A.; Fagherazzi, S. Morphological barrier island changes and recovery of dunes after Hurricane Dennis, St. George Island, Florida. *Geomorphology* **2010**, *114*, 614–626. [CrossRef]
26. Bochev-Van der Burgh, L.M.; Wijnberg, K.M.; Hulscher, S.J.M.H. Decadal-scale morphologic variability of managed coastal dunes. *Coast. Eng.* **2011**, *58*, 927–936. [CrossRef]
27. Richter, A.; Faust, D.; Maas, H.G. Dune cliff erosion and beach width change at the northern and southern spits of Sylt detected with multi-temporal Lidar. *Catena* **2013**, *103*, 103–111. [CrossRef]

28. Barber, D.M.; Mills, J.P. Vehicle based waveform laser scanning in a coastal environment. In Proceedings of the 5th International Symposium on Mobile Mapping Technology, Padua, Italy, 29–31 May 2007; Volume 36, p. C55.
29. Bitenc, M.; Lindenbergh, R.; Khoshelham, K.; Van Waarden, A.P. Evaluation of a LIDAR Land-Based Mobile Mapping System for Monitoring Sandy Coasts. *Remote Sens.* **2011**, *3*, 1472–1491. [CrossRef]
30. Aagaard, T.; Kroon, A.; Andersen, S.; Sørensen, R.M.; Quartel, S.; Vinther, N. Intertidal beach change during storm conditions; Egmond, The Netherlands. *Mar. Geol.* **2005**, *218*, 65–80. [CrossRef]
31. Van Enckevort, I.M.J.; Ruessink, B.G. Effect of hydrodynamics and bathymetry on video estimates of nearshore sandbar position. *J. Geophys. Res. Oceans* **2001**, *106*, 16969–16979. [CrossRef]
32. Glennie, C. Rigorous 3D error analysis of kinematic scanning LIDAR systems. *J. Appl. Geod.* **2007**, *1*, 147–157. [CrossRef]
33. Ruessink, B.G.; Arens, S.M.; Kuipers, M.; Donker, J.J.A. Coastal dune dynamics in response to excavated foredune notches. *Aeolian Res.* **2018**. [CrossRef]
34. Stockdon, H.F.; Holman, R.A.; Howd, P.A.; Sallenger, A.H., Jr. Empirical parameterization of setup, swash, and runup. *Coast. Eng.* **2006**, *53*, 573–588. [CrossRef]
35. Brakenhoff, L.B.; Smit, Y.; Donker, J.J.A.; Ruessink, B.G. Tide-induced variability in beach surface moisture: Observations and modelling. *Earth Surf. Process. Landf.* **2018**. [CrossRef]
36. Spencer, T.; Brooks, S.M.; Evans, B.R.; Tempest, J.A.; Möller, I. Southern North Sea storm surge event of 5 December 2013: Water levels, waves and coastal impacts. *Earth-Sci. Rev.* **2015**, *146*, 120–145. [CrossRef]
37. Van de Graaff, J. Dune erosion during a storm surge. *Coast. Eng.* **1977**, *1*, 99–134. [CrossRef]
38. Vellinga, P. Beach and dune erosion during storm surges. *Coast. Eng.* **1982**, *6*, 361–387. [CrossRef]
39. Saarinen, N.; Vastaranta, M.; Vaaja, M.; Lotsari, E.; Jaakkola, A.; Kukko, A.; Kaartinen, H.; Holopainen, M.; Hyyppä, H.; Alho, P. Area-based approach for mapping and monitoring riverine vegetation using mobile laser scanning. *Remote Sens.* **2013**, *5*, 5285–5303. [CrossRef]
40. Harding, D.J.; Lefsky, M.A.; Parker, G.G.; Blair, J.B. Laser altimeter canopy height profiles: Methods and validation for closed-canopy, broadleaf forests. *Remote Sens. Environ.* **2001**, *76*, 283–297. [CrossRef]
41. De Vries, S.; Southgate, H.N.; Kanning, W.; Ranasinghe, R. Dune behavior and aeolian transport on decadal timescales. *Coast. Eng.* **2012**, *67*, 41–53. [CrossRef]
42. Keijsers, J.G.S.; Poortinga, A.; Riksen, M.J.P.M.; Maroulis, J. Spatio-temporal variability in accretion and erosion of coastal foredunes in the netherlands: Regional climate and local topography. *PLoS ONE* **2014**, *9*, e91115. [CrossRef] [PubMed]
43. Pye, K.; Blott, S.J. Assessment of beach and dune erosion and accretion using LiDAR: Impact of the stormy 2013–14 winter and longer term trends on the Sefton Coast, UK. *Geomorphology* **2016**, *266*, 146–167. [CrossRef]
44. Psuty, N. The coastal foredune: A morphological basis for regional coastal dune development. In *Coastal Dunes*; Springer: Berlin/Heidelberg, Germany, 2008; pp. 11–27.
45. Hoonhout, B.M.; Vries, S.D. A process-based model for aeolian sediment transport and spatiotemporal varying sediment availability. *J. Geophys. Res. Earth Surf.* **2016**, *121*, 1555–1575. [CrossRef]
46. Davidson-Arnott, R.G.; Law, M.N. Seasonal patterns and controls on sediment supply to coastal foredunes, Long Point, Lake Erie. In *Coastal Dunes: Form and Process*; John Wiley & Sons: Hoboken, NJ, USA, 1990; pp. 177–200.
47. Delgado-Fernandez, I. Meso-scale modelling of aeolian sediment input to coastal dunes. *Geomorphology* **2011**, *130*, 230–243. [CrossRef]
48. OxTS. *RT Post-Process Wizard*; Oxford Technical Solutions Limited: Upper Heyford, UK, 2011.
49. Riegl LMS GmbH. *RiProcess Manual*; Riegl LMS GmbH: Horn, Austria, 2014.
50. *MATLAB*, Version 9.2.0 (R2017a); The MathWorks Inc.: Natick, MA, USA, 2017.
51. D'Errico, J. Inpain Nans. Matlab Central File Exchange, Release: 2, 2004. Available online: https://nl.mathworks.com/matlabcentral/fileexchange/4551-inpaint_nans (accessed on 19 July 2008). [CrossRef]
52. Rieger, P.; Studnicka, N.; Pfennigbauer, M.; Zach, G. Boresight alignment method for mobile laser scanning systems. *J. Appl. Geod.* **2010**, *4*, 13–21.